Publ. Astron. Soc. Japan **43**, 381–411 (1991)

Two-Dimensional Inversion for Solar Internal Rotation

Takashi SEKII

Department of Astronomy, Faculty of Science, The University of Tokyo, Bunkyo-ku, Tokyo 113

(Received 1990 June 29; accepted 1991 March 6)

Abstract

The internal rotation of the sun is inferred by solving a fully two-dimensional inverse problem of the rotational splitting data of Libbrecht (1989, AAA 080.006). We solve a set of integral equations which relate the rotational splittings of the eigenfrequencies of the sun to the internal rotation rate of the sun, the latter being considered as a function of both the distance from the center and the latitude. For this purpose we suggest an inverse method and apply it to the present problem. The integral equations are descretized and reduced to a set of linear equations. First, we impose an error-weighted least-squares condition with some boundary constraints at the surface. Second, we impose a flatness condition: the average of the first derivatives of the rotation rate is required to be as small as possible under the first constraint. Inversions were carried out while fully utilizing singular-value decomposition. In order to stabilize the solution to observational and numeric errors, we discarded small singular values. The results of numerical experiments show that the best resolution is obtained within a depth range of $0.6 \lesssim r/R \lesssim 0.9$ in the low-latitude region. By inverting the observed splittings, we found that the solar internal rotation in the low-latitude region is slightly faster than the surface rotation rate in the outer ten percent of the radius, and decreases to about five percent less than the surface rotation rate within the lower levels of the convection zone. In the region $0.7 \lesssim r/R \lesssim 0.8$, the rotation rate within the low-latitude zone is as fast as the surface rate, but is slower than the surface rate at $r/R \lesssim 0.7$. The rotation rate within the mid-latitude region decreases with depth in the outer twenty percent of the radius, and gradually increases inward to be faster than the surface rate.

Key words: Solar oscillations; Solar rotation; Sun.

1. Introduction

The internal rotation or the internal magnetic field of the sun introduces a specific direction to the figure of the sun, and generates a fine structure of the eigenfrequency spectrum, which is often quoted as frequency splittings. Without any rotation or magnetic field, the oscillation frequencies depend only on the spherical harmonic degree, l, and radial order, n; it is said that the spectrum is degenerate with respect to azimuthal order m. Once even slow rotation appears in the system, however, the degeneracy is resolved and each (l, n) multiplet is split into $(2l+1)$ distinct singlet frequencies each with a different azimuthal order m. Solar rotation is assumed to be sufficiently slow that we can apply the above-mentioned picture.

The form of the sun's internal angular velocity is of great importance to understanding solar activity; yet, there is still no reliable theory to predict it. Helioseismic approaches are thus important as unique tools for providing experimental data. To measure the rotational splittings of the eigenfrequencies, a highly precise measurement of the eigenfrequencies is required, since the frequency splitting is of the order of magnitude of the solar rotation rate, which at the equator is about 460 nHz at the surface. The first success was to measure the frequency splittings of the sectral modes $(|m| = l)$, which are, roughly speaking, $2l$-times greater than the surface rotation rate (Duvall and Harvey 1984). Since the sectorial modes are confined to within the low-latitude zones, these data provide us with information about the internal rotation near the equatorial plane (Duvall et al. 1984; Gough 1984). Recently, fully two-dimensional observations of the solar disk have been made by various observers. These enable us to infer both the radial and latitudinal variation of solar internal rotation; indeed, some attempts have already been made (Christensen-Dalsgaard and Schou 1988; Korzennik et al. 1988, 1990; Rhodes et al. 1988, 1990; Brown et al. 1989; Dziembowski et al. 1989; Goode et al. 1990; Sekii 1990).

Several methods to invert rotational splitting data have been suggested, and have been applied to both one- and two-dimensional cases. The first attempt to perform fully two-dimensional inversion was carried out by Sekii (1990). In the present paper we present details concerning a method which was briefly described by Sekii (1990), and apply it to the observational frequency-splitting data of Libbrecht (1989).

In section 2, the inverse problem for rotational splitting is discussed. We describe a new inversion method based on an algebraic treatment in section 3. It is applied to the observed splitting data (Libbrecht 1989) in section 4. The results are presented in section 5, and are discussed in section 6.

2. Inverse Problem of Rotational Splittings

In this section we formulate the inverse problem for rotational splitting, and review some techniques which are closely related to the method presented in section 3. Excellent reviews of inverse problems have been presented by Parker (1977) and Gough (1985) from geophysical and helioseismological points of view, respectively. A rather mathematical review was presented in a monograph by Craing and Brown (1986).

2.1. Integral Equation

When a star rotates, the degeneracy of its eigenfrequencies with respect to the azimuthal order, m, is lifted, where the azimuthal angle is measured around the rotation axis. The effect of rotation on the eigenfrequencies observed from an inertial frame is given approximately by (e.g., Hansen et al. 1977)

$$\omega_{nlm} - \omega_{nl0} = m\left[\int_0^R \{U_{nl}(r)^2 + l(l+1)V_{nl}(r)^2\}\rho(r)r^2dr\right]^{-1}$$
$$\times\frac{2l+1}{2}\frac{(l-|m|)!}{(l+|m|)!}\int_0^R dr\int_0^\pi \sin\theta d\theta\rho r^2\Omega(r,\theta)$$
$$\times\left[\{U_{nl}(r)^2 - 2U_{nl}(r)V_{nl}(r)\}P_l^m(\cos\theta)^2\right.$$
$$+V_{nl}(r)^2\left\{\frac{m^2}{\sin^2\theta}P_l^m(\cos\theta)^2 - 2\ fraccos\theta\sin\theta P_l^m(\cos\theta)\frac{dP_l^m(\cos\theta)}{d\theta}\right.$$
$$\left.\left.+\left(\frac{dP_l^m(\cos\theta)}{d\theta}\right)^2\right\}\right], \tag{2.1}$$

provided that the rotation is slow enough for the effects of the higher-order terms of the rotation, Ω, on the oscillation to be negligible. Here, ω_{nlm} is the eigenfrequency under the effect of angular velocity, $\Omega(r,\theta)$; $U_{nl}(r)$ and $V_{nl}(r)$ are the radial parts of the displacement eigenfunction in the case of no rotation; and $P_l^m(\cos\theta)$ denotes the associated Legendre function. Hereafter, we write equation (2.1) symbolically as

$$\delta\omega_{nlm} = \int_0^R\int_0^\pi K_{nlm}(r,\theta)\Omega(r,\theta)drd\theta. \tag{2.2}$$

The function $K_{nlm}(r,\theta)$ describes the sensitivity of an eigenmode to the angular velocity, $\Omega(r,\theta)$. It is dependent on the equilibrium structure of the star and on the eigenmodes under consideration, and is usually called the splitting kernel. We hereafter refer to $\delta\omega_{nlm} \equiv \omega_{nlm} - \omega_{nl}$ as the frequency splitting.

We can regard equation (2.2) as being an integral equation in which $\Omega(r,\theta)$ appears as an unknown function. If the rotational splittings, $\delta\omega_{nlm}$, are measured for many modes with different sets of quantum numbers $\{nlm\}$, we are provided with a set of integral constraints on Ω. To calculate the kernels, K_{nlm}, we require a spherically symmetric structure of the sun and the eigenfunctions in the case of no rotation. We usually adopt a standard solar model and its eigenfunctions for this purpose. In this sense, the problem is a linearization about the rotating solar model.

2.2. Mathematical Aspects of Linear Inverse Problems

The problem is to solve a set of linear integral equations (2.2). For the convenience of mathematical discussion, we rewrite equation (2.2) as

$$\int K_i(x)f(x)dx = g_i, \qquad i = 1,\ldots,M, \tag{2.5}$$

where f and g correspond to Ω and $\delta\omega$, respectively; suffix i represents $\{nlm\}$; $x \equiv (r,\theta)$; and M denotes the number of available modes.

The problem is how to recover function $f(x)$ from $\{g_i\}$. The first question is whether the solution exists or not. The solution may not exist if the equations are inconsistent with each other. Such a case may result from error contamination in the measurement of g_i; bad choices of the kernel functions, K_i; or an inappropriate numerical treatment of the problem. The answer to the question is not always known: it depends on the problem, on the procedure adopted, and on quality of data.

The second question is whether the solution is unique or not, even if it exists. The answer to that question is clear. If any solution is obtained, there are an infinite number of solutions. The problem is therefore ill posed.

2.3. Some Techniques for Solving Linear Inverse Problems

(1) Least-squares method based on singular-value decomposition

By replacing the integral in equation (2.5) with a summation, after discretizing the interval of the integral, we obtain a set of algebraic equations. The coefficients matrix is, in general, rectangular. To solve such a set of algebraic equations, we can use the least-squares method after decomposing the coefficients matrix by means of the singular-value decomposition technique (see Forsythe et al. 1977). Gabriel and Nemry (1986) applied this method to Duvall and Harvey's (1984) rotational-splitting data. Their case is one-dimensional, since they analyzed the rotation rate on the equatorial plane. The method that we desribe in the next chapter has an outlook which is similar to theirs.

(2) Regularization

In order to rule out physically unacceptable solutions, which result from large error magnification, we often adopt a regularization method (Phillips 1962, Twomey 1963, Tikhonov 1963). Accounting for the fact that an inverse problem does not always have a solution, our aim is generally to minimize

$$S \equiv \left| \int K_i(x) f(x) dx - g_i \right|^2 . \tag{2.6}$$

In the regularization method we minimize

$$S_\lambda \equiv \left| \int K_i(x) f(x) dx - g_i \right|^2 + \lambda |\mathcal{S} f|^2 \tag{2.7}$$

instead of S, where the operator $\mathcal{S}$ is some type of smoothing operator. In the limit $\lambda \to 0$, minimization of S_λ leads to a least-squares solution. For a large value of λ, on the other hand, we obtain a smoothed, stable solution due to the smoothing term. By increasing λ, although the solution is stabilized, the residual, S, increases. An application of this regularization method to helioseismic inversions has been discussed by Jeffrey (1988).

Christensen-Dalsgaard and Schou (1988), Dziembowski et al. (1989), Goode et al. (1990), and Korzennik et al. (1990) adopted this method to invert frequency splittings in order to determine solar rotation. They expanded $\Omega(r, \theta)$ as

$$\Omega(r, \theta) = \Omega_0(r) + \Omega_2(r) \cos^2 \theta + \Omega_4(r) \cos^4 \theta \tag{2.8}$$

and searched for functions $\Omega_0(r), \Omega_2(r)$ and $\Omega_4(r)$ which minimizes S_λ, with $\mathcal{S}$ being chosen so as to suppress any derivatives of those functions. Since they ignored higher-order terms [$\Omega_6(r)\cos^6\theta,\ldots$], their treatment imposes a fairly smooth change of $\Omega(r,\theta)$ with θ, while allowing a strong r dependence. This is justified by the fact that the current data for splittings are usually presented in some form of expansions related to expansion (2.8), in which higher terms are not presented because of a lack of accuracy.

Our approach is different from theirs regarding two points: First, we do not adopt expansion (2.8), which is well justified in the context of analyzing current splitting data. Instead, we perform direct gridding. In the near future when we try to include higher-order terms of expansion (2.8), provided with data of higher accuracy, direct gridding will be preferred to adding more terms to expansion (2.8), though it is not presently clear how significant the higher terms are to what kind of problems (cf. Stenflo 1989). Besides, direct gridding provides us with a simpler formulation when we wish to suppress some derivative of Ω, itself. Second, we utilize a hybrid inversion scheme, which uses singular-value decomposition supplemented by regularization based on flatness. Details are presented in the next section.

3. An Extension of the Least-Squares Method

3.1. Posing of the Problem

In this chapter we describe the inverse method adopted in the present work. We suppose that the rotation is dependent on both r (the distance from the center) and the colatitude, θ. We seek $\Omega(r,\theta)$ subject to a set of constraints (2.1) or, equivalently,(2.2) for various values of $\{nlm\}$. We replace the integral in equation (2.2) with a summation by discretization, and derive

$$\delta\omega_{wlm} = \sum_{I=1}^{N_1}\sum_{J=1}^{N_2} K_{nlm}(r_I,\theta_J)\Omega(r_I,\theta_J)\Delta r_I \Delta\theta_J. \tag{3.1}$$

Here, N_1 and N_2 are the numbers of radial and angular mesh points, respectively, and r_I and θ_J denote the I-th radial mesh point and the J-th angular mesh point, respectively. It is convenient to introduce single indices which specify the mode and the mesh point, leading to equation

$$\delta\omega_i = \sum_{j=1}^{N} K_{ij}\Omega_j, \quad i=1,\ldots,M. \tag{3.2}$$

Here, i and j are the index for the modes labeled by $\{nlm\}$ and that for the mesh points labeled by I and J, respectively; we have introduced

$$K_{ij} \equiv K_{nlm}(r_I,\theta_J)\Delta r_I \Delta\theta_J \tag{3.3}$$

and

$$\Omega_j \equiv \Omega(r_I,\theta_J). \tag{3.4}$$

Hereafter, suffix i indicates that the quantity belongs to the i-th mode, and suffix j indicates the quantity is measured at the j-th mesh point. M is the number of modes considered, and $N = N_1 \times N_2$ is the number of mesh points. Equation (3.2) can be transformed into the following algebraic formula:

$$\boldsymbol{e} = \boldsymbol{K\Omega}, \tag{3.5}$$

where

$$\boldsymbol{e} \equiv (\delta\omega_i), \quad \boldsymbol{\Omega} \equiv (\Omega_j), \quad \boldsymbol{K} = (K_{ij}). \tag{3.6}$$

Note that the sizes of $\boldsymbol{e}$, $\boldsymbol{\Omega}$ and $\boldsymbol{K}$ are $M \times 1, N \times 1$, and $M \times N$, respectively. The problem now turns to how to solve the algebraic equation (3.5).

3.2. Treatment of the Least-Squares Equation

In this section we concentrate on the mathematical aspects of the problem. Let us consider linear equation (3.5). Both the existence and uniqueness of the solution depend on the size of the matrix, on the rank r of the matrix, and on the consistency of the data $\boldsymbol{e}$, which may be destroyed by error contamination. The consistency of the data would matter only in a case where $r < M$, in which the number of data is greater than the number of independent data, i.e., the data set is redundant and, hence, has a possibility of being inconsistent. If $r = N$, the number of unknown quantities is identical to the number of independent data. Even in this case, data inconsistency may occur if $r < M$; in such a case a least-squares approximation is often adopted. If $r < N$, the number of the unknown quantities is greater than the number of the independent data, and we cannot expect a unique solution. This non-uniqueness appears even if we seek a least-squares approximation when data inconsistency occurs.

When there is no unique solution, some additional conditions must be imposed in order to select a solution or a least-squares approximation among various possible candidates. A well-known treatment is to choose the solution of minimal norm among an infinite number of solutions or least-squares solutions, i.e., to choose $\boldsymbol{\Omega}_{LSMN}$ which minimizes $|\boldsymbol{\Omega}|^2$. The solution, thus determined, is called the least-squares minimal norm solution of equation (3.5). In practical applications we do not always prefer the least-squares minimal norm solution to other possible solutions. It is a well established process, however, to find the least-squares minimal norm solution of a linear equation through singular value decomposition.

In general, a matrix $\boldsymbol{K}$ can be uniquely expressed by means of the singular-value decomposition (see Forsythe et al. 1977), in which $\boldsymbol{K}$ is written as

$$\boldsymbol{K} = \boldsymbol{U\Sigma V}^T, \tag{3.7}$$

where $\boldsymbol{U}$ and $\boldsymbol{V}$ are unitary matrices of sizes $M \times M$ and $N \times N$, respectively, and $\boldsymbol{\Sigma}$ is a diagonal matrix of size $M \times N$. The diagonal components of the matrix Σ are the singular values of the matrix $\boldsymbol{K}$:

$$\Sigma_{ij} = \begin{cases} \sigma_i\delta_{ij}, & \text{if } 1 \le i \le r; \\ 0, & \text{otherwise,} \end{cases} \tag{3.8}$$

with

$$\sigma_1 \geq \sigma_2 \geq \cdots \geq \sigma_r > 0. \tag{3.9}$$

Here, δ_{ij} is the Kronecker delta and σ_i are singular values of the matrix (see Forsythe et al. 1977). By the variable transformation $\boldsymbol{\Omega}' \equiv \boldsymbol{V}^T\boldsymbol{\Omega}$ and $\boldsymbol{e}' \equiv \boldsymbol{U}^T\boldsymbol{E}$ equation (3.5) is transformed to

$$\boldsymbol{\Sigma}\boldsymbol{\Omega}' = \boldsymbol{e}', \tag{3.10}$$

whose components are

$$\begin{aligned}
\sigma_1 \Omega_1' &= e_1' \\
\sigma_2 \Omega_2' &= e_2' \\
&\vdots \\
\sigma_r \Omega_r' &= e_r' \\
0 &= e_{r+1}' \\
&\vdots \\
0 &= e_M'.
\end{aligned} \tag{3.11}$$

From this we obtain

$$\Omega_i' = e_i'/\sigma_i \quad (1 \leq i \leq r); \tag{3.12}$$

Ω_i' is arbitrary for $r+1 < i < N$. Note that $\boldsymbol{\Omega}'$, thus obtained, does not generally satisfy equation (3.11), since it is possible that some of the $e_i'(r+1 < i < M)$ are non-zero. Thus, $\boldsymbol{\Omega}'$ should generally be called the least-squares solution of equation (3.11).

Since a unitary transformation maintains the norm unchanged, the norm of vector Ω becomes minimum if we set $\boldsymbol{\Omega}_i' = 0$ for $r+1 < i < N$; i.e.,

$$\Omega_i' = \begin{cases} b_i'/\sigma_i, & \text{if } 1 \leq i \leq r; \\ 0, & \text{otherwise,} \end{cases} \tag{3.13}$$

or

$$\boldsymbol{\Omega}' = \boldsymbol{\Sigma}^\dagger \boldsymbol{e}', \tag{3.14}$$

where

$$\Sigma_{ij}^\dagger \equiv \begin{cases} \sigma_i^{-1}\delta_{ij}, & \text{if } 1 \leq i \leq r; \\ 0, & \text{otherwise.} \end{cases} \tag{3.15}$$

Then, the least-squares minimal norm solution $\boldsymbol{\Omega}_{LSMN}$ is given by

$$\begin{aligned}
\boldsymbol{\Omega}_{LSMN} &= \boldsymbol{V}\boldsymbol{\Sigma}^\dagger \boldsymbol{U}^T \boldsymbol{e} \\
&\equiv \boldsymbol{K}^\dagger \boldsymbol{e}.
\end{aligned} \tag{3.16}$$

The matrix $\boldsymbol{K}^{\dagger}$ is called the Moore-Penrose generalized inverse matrix of $\boldsymbol{K}$, though the definition of the Moore-Penrose generalized inverse matrix is given in a different form in mathematics (e.g., Rao and Mitra 1971).

We now turn to other possible solution of equation (3.11). The fact that Ω_i' is arbitrary for $r+1<i<N$ gives us a relation between a least-squares solution $\boldsymbol{\Omega}_{LS}$ and another one $\boldsymbol{\Omega}_0$,

$$\boldsymbol{\Omega}_{LS}=\boldsymbol{\Omega}_0+\boldsymbol{V}^T\boldsymbol{u}, \tag{3.17}$$

where $\boldsymbol{u}$ is an $N\times 1$ vector comprising

$$\boldsymbol{u}=\begin{pmatrix}0\\ \vdots\\ 0\\ \boldsymbol{u}_c\end{pmatrix} \tag{3.18}$$

and $\boldsymbol{u}_c$ is an arbitrary vector of size $N-r$. If we obtain one least-squares solution, $\boldsymbol{\Omega}_0$, we can obtain another least-squares solution by changing the components of vector $\boldsymbol{u}_c$. Vector $\boldsymbol{u}$ belongs to the annihilator of matrix $\boldsymbol{K}$ and, thus, adding $\boldsymbol{V}^T$ $\boldsymbol{u}$ does not affect the residual of the equation.

We now extend this process to replace the norm by a general quadratic form (Sekii and Shibahashi 1988); i.e., to choose a solution which minimizes

$$S_D\equiv(\boldsymbol{\Omega},\boldsymbol{D\Omega}). \tag{3.19}$$

Here, the parentheses indicate the inner product an D is and $N\times N$ hermitian matrix. If matrix D is the unit matrix, S_D is $|\boldsymbol{\Omega}|^2$ and the solution sought is identical to the least-squares minimal norm solution.

The next task is to find a vector $\boldsymbol{u}_c$ minimizes S_D:

$$\partial S_D/\partial\boldsymbol{u}_c=0. \tag{3.20}$$

Note that

$$\begin{aligned}S_D&=(\boldsymbol{\Omega},\boldsymbol{D\Omega})\\ &=(\boldsymbol{\Omega}',\boldsymbol{D}'\boldsymbol{\Omega}')\end{aligned} \tag{3.21}$$

with $\boldsymbol{D}'=\boldsymbol{V}^T\boldsymbol{D}\boldsymbol{V}$ and

$$\partial S_D/\partial\boldsymbol{\Omega}'=2\boldsymbol{D}'\boldsymbol{\Omega}'. \tag{3.22}$$

This leads to

$$\sum_{j=r+1}^{N}D_{ij}'(u_c)_j=-\sum_{j=1}^{N}D_{ij}'\Omega_j',\quad i=r+1,\ldots,M. \tag{3.23}$$

After some manipulation, we obtain

$$\boldsymbol{u}_c = -\boldsymbol{D}_C'^{-1}\boldsymbol{D}_L'\boldsymbol{V}^T\boldsymbol{\Omega}_0, \tag{3.24}$$

where

$$\boldsymbol{D}_C' = \begin{pmatrix} D'_{r+1,r+1} & \cdots & D'_{r+1,N} \\ \vdots & \ddots & \vdots \\ D'_{N,r+1} & \cdots & D'_{NN} \end{pmatrix} \tag{3.25}$$

and

$$\boldsymbol{D}_L' = \begin{pmatrix} D'_{r+1,1} & \cdots & D'_{r+1,N} \\ \vdots & \ddots & \vdots \\ D'_{N,1} & \cdots & D'_{NN} \end{pmatrix}. \tag{3.26}$$

The combination of equations (3.17), (3.18), and (3.24) gives an $\boldsymbol{x}_{LSMS}$ which minimizes S_D while satisfying the least-squares equation (Sekii and Shibahashi 1988):

$$\boldsymbol{\Omega}_{LSMS} = \boldsymbol{V}(\boldsymbol{I}_N - \boldsymbol{I}_{N,N-r}\boldsymbol{D}_C'^{-1}\boldsymbol{D}_L')\boldsymbol{V}^T\boldsymbol{\Omega}_0, \tag{3.27}$$

where $\boldsymbol{I}_N$ is the $N \times N$ unit matrix, and $\boldsymbol{I}_{N,N-r}$ is an $N \times (N-r)$ matrix of the form

$$\boldsymbol{I}_{N,N-r} = \begin{pmatrix} \boldsymbol{O}_{r,N-r} \\ \boldsymbol{I}_{N-r} \end{pmatrix}. \tag{3.28}$$

Although $\boldsymbol{\Omega}_{LSMS}$ might seem to be fully dependent on the choice of $\boldsymbol{\Omega}_0$, It actually depends only on the first r components of $\boldsymbol{V}^T\boldsymbol{\Omega}_0$, which are common in all of the least-squares solutions. If we adopt $\boldsymbol{\Omega}_{LSMN}$ as $\boldsymbol{\Omega}_0$ to find $\boldsymbol{\Omega}_{LSMS}$, the burden of the computation is somewhat lightened since the upper limit of the summation in the right hand side of equation (3.22) is reduced to r. Numerically, however, it is safe to suppose that we cannot start exactly from $\boldsymbol{\Omega}_{LSMN}$. Such an attitude is necessary, particularly for cases in which we carry out some iterative improvement process which decreases the residual, but increases the norm.

3.3. An Extended Least-Squares Method in Helioseismic Inversion

An undesirable feature of matrix $\boldsymbol{K}$, which contains the splitting kernel, is that it often becomes nearly singular. In other words, the ratio of the largest singular value, σ_1, to the smallest singular value, σ_r, is large. Matrix $\boldsymbol{K}$ is usually non-singular mathematically and $r = \min(M, N)$. We should, however, discard those singular values which are much smaller than σ_1 in order to obtain a stable solution. This reduces the rank, and the problem becomes essentially underdetermined, since $r_{\mathrm{num}} < \min(M, N)$, where r_{num} is the the reduced rank. This would not be the case if the splitting kernels were sharply localized, and had similar amplitudes. The true splitting kernels, however, show a highly oscillatory behavior in the outer part of the sun, and overlap each other; the linear independence of the kernels is nearly broken there.

Another problem is error contamination. Besides purely numerical errors, data cannot be free from observational errors. Some errors also appear when integral equations are discretized. We should therefore not expect a vector $\boldsymbol{\Omega}$ which satisfies equation (3.5) exactly, and should seek least-squares solutions, even if they are not uniquely determined.

One might hope that a redistribution of the mesh points could recover the linear independence of the kernels and, hence, non-singularity of matrix $\boldsymbol{K}$. This, however, is a difficult task to complete if the number of mesh points and the number of modes are large. Since no algorithm is known which can carry out such a task systematically, the approach inevitably includes some extent of trial-and-error.

The problem of discretization errors is really profound. In the last section we stated that an inverse problem of continuous variables has no unique solution. Discretization could evade this non-uniqueness, by reducing the number of mesh points to the number of data, while keeping matrix $\boldsymbol{K}$ non-singular. However, if we try to suppress discretization errors, we cannot reduce the number of mesh points freely. Keeping the discretization error to a certain level, we cannot always have a non-singular matrix $\boldsymbol{K}$. The problem has nothing to do with the problem of error contamination or bad behavior of splitting kernels, but of misrepresenting the solution.

In the previous section we described how to select among the least-squares solutions one that minimizes a quadratic form. If we set the matrix $\boldsymbol{D}$ properly, $S_{\boldsymbol{D}}$ becomes a discretized version of some measure of smoothness, or flatness, of the function $\Omega(r,\theta)$. For example, we define the flatness, S_F, by

$$S_F = \int_0^R r dr \int_0^\pi d\theta |\nabla \Omega(r,\theta)|^2. \tag{3.29}$$

If we obtain discretized expression of S_F as a quadratic form, S_D, with some coefficients, Q_{ij}, as

$$S_D = \sum_{i,j=1}^{N} Q_{ij}\Omega_i\Omega_j, \tag{3.30}$$

matrix $\boldsymbol{D}$ is obtained by

$$D_{ij} = \frac{1}{2}(Q_{ij} + Q_{ji}). \tag{3.31}$$

The form of S_D is obtained from the equality

$$S_F = \int_0^R r dr \int_0^\pi d\theta \left[\left(\frac{\partial \Omega}{\partial r}\right)^2 + \frac{1}{r^2}\left(\frac{\partial \Omega}{\partial \theta}\right)^2\right] \tag{3.32}$$

as

$$S_D = \sum_{I=1}^{N_1-1}\sum_{J=1}^{N_2-1} g_{IJ}\Delta S_{IJ}, \tag{3.33}$$

where

$$\Delta S_{IJ} = \frac{r_I + r_{I+1}}{2}(r_{I+1} - r_I)(\theta_{J+1} - \theta_J) \tag{3.34}$$

and

$$g_{IJ} = \frac{1}{2}\frac{(\Omega_{I+1,J}-\Omega_{I,J})^2+(\Omega_{I+1,J+1}-\Omega_{I,J+1})^2}{(r_{I+1}-r_I)^2} + \frac{1}{2}\left(\frac{2}{r_I+r_{I+1}}\right)^2 \frac{(\Omega_{I,J+1}-\Omega_{I,J})^2+(\Omega_{I+1,J+1}-\Omega_{I+1,J})^2}{(\theta_{J+1}-\theta_J)^2}. \tag{3.35}$$

Here, to be concise, Ω has two indices, I and J, as the radial and angular mesh indicators. It is easy to unify indices I and J to a single index, in order to obtain a formula with the same structure as equation (3.2); we can thus calculate the coefficients Q_{ij}. Equation (3.33) gives an algorithm for computing Q_{ij}.

Note that any matrix $\boldsymbol{D}$ that gives a quadratic form for flatness is singular. This results from the fact that one cannot reconstruct a function from only its gradient, i.e., equation $\boldsymbol{Dx}=\boldsymbol{b}$ has an infinite number of solutions. Hence, although matrix $\boldsymbol{D}'$ is also singular, matrices $\boldsymbol{D}'_C$ and $\boldsymbol{D}'_L$ are non-singular, reflecting the fact that once we know Ω at even one point, we can derive Ω, itself, from its gradient, $\nabla\Omega$.

We should next refer to the trade-off appearing in the present algorithm. It appears in the process through the criterion for the lower limit of singular values. Practically, we introduce a parameter, ε, and discard any singular values σ_i if $\sigma_i < \varepsilon\sigma_1$. If we set ε to be nearly unity, only a few singular values are obtained and, hence, only a few features associated with those singular values can be significantly recovered. In this case, some features are lost and the residual of the equation becomes large; it may be inappropriate to call the resulting representation a solution. On the other hand, if we make ε too small, error magnification becomes too large. There is no objective criterion for choosing ε.

The algorithm described above is summarized as follows. We first carry out a singular-value decomposition of the kernel matrix, and then calculate the least-squares minimal norm solution. Here, we first discard small singular values by some criterion. We then construct a matrix which gives a flatness measure of the solution. By adding the vector derived from the matrix to the least-squares minimal norm solution, we eventually obtain a solution which is the flattest among the least-squares solutions.

Mathematically, the summary given above is described as follows. First, utilizing singular value decomposition, we separate out the subspace spanned by the row vectors of kernel matrix $\boldsymbol{K}$ from the total N-dimensional space. In this space we search for a vector that satisfies the algebraic equation. We then add a vector which belongs to the annihilator in order to obtain the flatness of the solution.

It is worth mentioning the difference between the present method and standard regulalization methods which were described in the last chapter. Whatever measure we adopt as smoothness, the standard regularization tends to suppress any features which are not smooth. On the other hand, the present method allows any wild feature as long as it results from some equation associated with a large singular value.

In the next section an application of the present method to observed frequency splitting data is described.

4. Preparation for Inversion of Observed Frequency Splittings

We apply our inversion method to the rotational splitting data of Libbrecht (1989). Like the other attempts made along this line so far made, we assume that standard solar models are sufficiently good and we adopt model 1 of Shibahashi et al. (1983) in order to calculate the splitting kernels. This assumption is supported by the inversions of the p-mode frequencies to infer the equilibrium structure of the sun (e.g., Christensen-Dalsgaard et al. 1985, 1988; Gough and Kosovichev 1988; Shibahashi and Sekii 1988; Vorontsov 1988; Vorontsov and Shibahashi 1990; Dziembowski et al. 1990).

4.1. Data

Libbrecht (1989) presented his observational results of the solar p-mode frequency splittings, based on 100 days of solar Doppler observations from Big Bear Solar Observatory. The observation was operated in 1986 between March 26 and August 2, at the minimum phase of solar activity. The red and blue wings of the 6439 Å calcium line were observed. He expanded the observed frequency splittings in the form

$$\delta\omega_{nlm} = l\sum_{i=1}^{5} a_i P_i(m/l), \tag{4.1}$$

where P_i is the Legendre polynomial of the i-th degree, and tabulated the coefficients, a_i, for $5 < l < 60$ and their standard deviations. We computed each $\delta\omega_{nlm}$ again from the coefficients with the estimated error. Since no rotation rate would yield an even-order coefficient to the first order, we picked out only the odd-order coefficients: only a_1, a_3, and a_5 are included in the analysis. Thus, we calculated

$$\delta\omega_{mln} = l[a_1P_1(m/l) + a_3P_3(m/l) + a_5P_5(m/l)] \tag{4.2}$$

instead of evaluating equation (4.1), and estimated the statistical error $\Delta\delta\omega_{nlm}$ by the formula

$$\Delta\delta\omega_{nlm} = l\sqrt{[\delta a_1P_1(m/l)]^2 + [\delta a_3P_3(m/l)]^2 + [\delta a_5P_5(m/l)]^2}, \tag{4.3}$$

where δa_i is the uncertainty in a_i.

4.2. Splitting Kernels

We first solved the eigenvalue problem in order to obtain the eigenfunctions of the linear adiabatic oscillations of the model, $U_{nl}(r)$ and $V_{nl}(r)$. A fourth-order differential equation was solved by the method outlined in Unno et al. (1989), using 492 mesh points. The splitting kernels were then computed following equation (2.1). The associated Legendre functions were computed by an algorithm almost identical to that used by Libbrecht (1985).

4.3. Discretization

In the present analysis the number of radial and angular mesh points, N_1 and N_2, were chosen to 100 and 20, respectively. If we make the mesh finer, the memory size of the computer that we are now using limits the number of modes which can be treated. On the other hand, if we make the mesh coarser, the discretization error becomes large and the eigenfunctions cannot be properly treated. The mesh points were distributed such that the spacing was smaller in both the outer region (radial) and at low latitudes. Apparently, the resolution is poor for high-latitude zones. The reason for such a choice of angular mesh is that we decided to concentrate on low- to mid-latitude zones, since the most precisely measured data are for sectoral modes which have large amplitudes, mainly in the vicinity of the equatorial plane.

We discretize any integral J of the type

$$J = \int_{r_1}^{r_2} r dr \int_{\theta_1}^{\theta_2} d\theta F(r,\theta) \tag{4.4}$$

as

$$J_D \equiv \sum_{I=1}^{N_1-1} \sum_{J=1}^{N_2-1} \bar{F}_{IJ} \Delta S_{IJ} \tag{4.5}$$

with

$$\bar{F}_{IJ} \equiv \frac{1}{4}(F_{I,J} + F_{I,J+1} + F_{I+1,J} + F_{I+1,J+1}) \tag{4.6}$$

and

$$\Delta S_{IJ} \equiv \frac{1}{2}(r_{I+1}^2 - r_I^2)(\theta_{J+1} - \theta_J), \tag{4.7}$$

where suffix I indicates the radial position and suffix J the angular position. It is easy to reduce equation (4.5) to the form

$$J_D = \sum_{i=1}^{N_1,N_2} c_i F_i, \tag{4.8}$$

where the mesh indices are unified to a single index, i.

Given the mesh system and the manner of discretization, one can test how well the linear integral equation is approximated by the discretized equation. We estimated the radial and the angular discretization errors separately by performing the following integrals:

$$I_1 = \int_0^R \rho r^2 [U_{nl}(r)^2 + l(l+1)V_{nl}(r)^2] dr, \tag{4.9}$$

$$I_2 = \int_0^R \rho r^2 [2U_{nl}(r)V_{nl}(r) + V_{nl}(r)^2] dr, \tag{4.10}$$

$$J_I = \int_0^\pi P_l^m(\cos\theta)^2 \sin\theta d\theta, \tag{4.11}$$

and

$$J_2 = \int_0^{\pi} \left[\frac{m^2}{\sin^2\theta} P_l^m(\cos\theta)^2 + \left\{ \frac{dP_l^m(\cos\theta)}{d\theta} \right\}^2 \right] \sin\theta d\theta. \tag{4.12}$$

Integrals I_1 and I_2 were evaluated with the present mesh size and compared with those computed using 492 radial mesh points; J_1 and J_2 were compared with the analytically obtained values. Integrals I_1 and I_2 were evaluated for each pair of l and n. From the result, we selected modes for which the integrals are computed to an accuracy better than two percent, which is comparable with the typical error contained in the data. Independently, integrals J_1 and J_2 were evaluated for every pair of l and m. Though it is clear that J_1 and J_2 cannot be evaluated properly using 20 angular mesh points (if $l-m$ exceeds 20), this test yields more quantitative information about whether an eigenmode of (l, m) can be included in the present analysis or not. As was anticipated, eigenmodes with small m were rejected.

In all, 1053 eigenmodes of various quantum numbers $\{lmn\}$ were chosen. The averaged uncertainty of the observed data chosen was about 2.6 percent. Thus, the discretization error in our system is comparable with, or less than, the observational error. Note that the present problem is underdetermined, since the number of mesh points is about twice as great as the number of modes.

We next divided each of equations by the data error: that is, we performed the replacements

$$\delta\omega_i \rightarrow \frac{\delta\omega_i}{\Delta\delta\omega_i} \tag{4.13}$$

and

$$K_{ij} \rightarrow \frac{K_{ij}}{\Delta\delta\omega_i} \tag{4.14}$$

in equation (3.2). Here, $\Delta\delta\omega_i$ denotes the statistical error contained in the measurement of $\delta\omega_i$. We thus obtain a set of error-weighted equations, in which each datum has an uncertainty of the order of unity.

4.4. Surface Boundary Constraint

We imposed a boundary constraint on the rotation rate. At the surface, we require the rotation rate to be close to the rate observed by Snodgrass (1983). In his work the relation between the rotation rate, Ω_s, and the latitude, ϕ, were studied from the motion of the magnetic field pattern. He represented his result in the following form:

$$\Omega_s(\phi) = A + B\sin^2\phi + C\sin^4\phi \tag{4.15}$$

where

$$A = 461.9 \pm 0.3, \tag{4.16}$$

$$B = -73.8 \pm 2.9, \tag{4.17}$$

and

$$C = -52.2 \pm 4.6, \tag{4.18}$$

where the unit is nHz. The boundary constraint was imposed at all 20 mesh points on the surface:

$$\Omega_i = \Omega_s(\theta_J), \quad J = 1, \ldots, N_2, \tag{4.19}$$

where $i = N_1 \times J$ and Ω_s is rewritten as a function of the colatitude. We again divided both sides of the equation by the estimated error in the observed surface rotation rate. The constraint equations were simply added to the equations for the frequency splittings to form matrix $\boldsymbol{K}$.

There are some reports on the surface rotation rate other than that of Snodgrass (1983). For example, Howard et al. (1983) observed the Doppler shift on the solar surface to derive the surface rotation law. Their results were somewhat different from Snodgrass's (1983), and the discrepancy has not been fully resolved. This could discourage merging an observed rotation rate with helioseismic data. However, while massive data of high-degree modes would enable us to investigate the dynamical structure near the surface, the present data provide splitting of degrees only up to 60. Thus, the outer region of the sun cannot be probed from only the present data, and we need some help from an observed rotation rate. Though the choice of the observed rotation rate is rather arbitrary, the choice does not affect the result in the deeper region.

Stenflo (1989) also used the magnetic field pattern as a tracer to derive the surface rotation law, which turned out to be different from that of Snodgrass. Stenflo's result is of particular interest since it includes the coefficients of $\sin^{2n}\phi$ with n up to 7, even though the higher coefficients are small. This suggests that the higher coefficients in expansion (2.8) may well have measurable, though small, amplitudes, at least at the surface.

4.5. Inversion of Matrices

To solve the set of linear equations given in equation (3.2) we adopted the algorithm described in section 3. We carried out a singular-value decomposition of matrix $\boldsymbol{K}$ by consecutively applying the Householder transformation (to obtain a bi-diagonal matrix) and the QR decomposition (to obtain a diagonal matrix). The trade-off parameter, ε, is taken into account in this step. We varied ε over a wide range. To obtain the final results, we should also compute the matrix $\boldsymbol{D}_C'^{-1}$ by applying the LU decomposition.

4.6. Statistical Error Estimation

In linear inverse problems, it is easy to follow the propagation of errors. Let us suppose that the solution of an algebraic equation is given in the form

$$\boldsymbol{x} = \boldsymbol{R}\boldsymbol{b}, \tag{4.20}$$

and the i-th component of vector $\boldsymbol{b}, b_i$, contains an error of δb_i. If

$$\langle \delta b_i \delta b_j \rangle = \delta_{ij} e_i^2, \tag{4.21}$$

where $\langle \cdots \rangle$ means an average, it is straightforward to evaluate the mean of the standard error in x_i as

$$\langle \delta x_i^2 \rangle = \sum_i e_j^2 R_{ij}^2. \tag{4.22}$$

If $e_j = 1$ for all j, as is the case in the error-weighted equation, equation (4.22) leads to

$$\langle \delta x_i^2 \rangle = \sum_j R_{ij}^2 = (\boldsymbol{R}\boldsymbol{R}^T)_{ii}. \tag{4.23}$$

The last term is the i-th diagonal component of matrix $\boldsymbol{R}\boldsymbol{R}^T$.

In the case of the least-squares minimal norm solution, $\boldsymbol{R} = \boldsymbol{V}\boldsymbol{\Sigma}^\dagger \boldsymbol{U}^T$ is obtained from equation (3.17), and we have

$$\langle \delta x^2_{LSMN,i} \rangle = \sum_{j=1}^{r} \left(\frac{V_{ij}}{\sigma_j} \right)^2 \tag{4.24}$$

for the least-squares minimal norm solution. It is simpler to consider that $\boldsymbol{x}'_{LSMN} \equiv \boldsymbol{V}^T \boldsymbol{x}_{LSMN}$ instead of $\boldsymbol{x}_{LSMN}$. Since $\boldsymbol{b}' = \boldsymbol{U}^T \boldsymbol{b}$, we obtain

$$\langle \delta b'_i \delta b'_j \rangle = \delta_{ij}. \tag{4.25}$$

From equation (3.15), we obtain

$$\langle \delta x'_{LSMSN,i} \delta x'_{LSMN,j} \rangle = \begin{cases} \delta_{ij}/\sigma_i, & (1 \le i \le r); \\ 0, & \text{otherwise}, \end{cases} \tag{4.26}$$

which corresponds to a generalized version of equation (4.24).

Then, we can estimate the error contained in $\boldsymbol{x}_{LSMS}$, if we replace $\boldsymbol{V}^T \boldsymbol{x}_0$ by $\boldsymbol{x}'_{LSMN}$ in equation (3.28),

$$\langle \delta x^2_{LSMS,i} \rangle = \sum_{j=1}^{r} \left(\frac{R_{ij}}{\sigma_j} \right)^2 , \tag{4.27}$$

where

$$\boldsymbol{R} = \boldsymbol{V}(\boldsymbol{I}_N - \boldsymbol{I}_{N,N-r} \boldsymbol{D}'^{-1}_C \boldsymbol{D}'_L). \tag{4.28}$$

5. Inverted Results

5.1. Inversions of Artificial Data

Before performing inversions of the observed data, we carried out numerical experiments to invert artificial data in order to confirm that the present inversion method works well to reproduce the rotation rate from the splittings data. These experiments inform us of the reliability of the inverted results of the real solar data. We computed two artificial splitting data sets for the modes included in the analysis for the rotation laws:

$$\Omega(r,\theta) = \Omega_{\rm eq}\left[\left(\frac{3}{2} - \frac{1}{2}\frac{r}{R}\right) - \frac{1}{4}\frac{r}{R}\cos^2\theta\right] \tag{5.1}$$

and

$$\Omega(r,\theta) = \Omega_{\rm eq}\left[1 + \frac{1}{5}\sin\left(10\pi\frac{r}{R}\right)\sin^2\theta\right]. \tag{5.2}$$

The factor $\Omega_{\rm eq}$ is the equatorial rotation rate at the surface, and is set as 462 nHz. Figures 1 and 2 show the model rotation rates given by equations (5.1) and (5.2), respectively. Hereafter, we call artificial data computed from rotation rate (5.1) artificial data 1, and those computed from rotation rate (5.2) artificial data 2. We first calculate the angular parts of equation (2.1) analytically, and then numerically integrate the radial parts using 492 mesh points. Although artificial data do not have any statistical uncertainty, we assumed that they do. That is, when we constructed kernel matrices, splitting kernels were weighted according to the virtual statistical error following (4.14). We considered two types of virtual errors: (1) one-percent relative errors to all the modes and (2) errors which are the same as those of the corresponding observed modes. In both cases, the error distribution is assumed to be Gaussian. In the case of type (1), we added those errors uniformly to all of the modes, although the observational errors are strongly dependent on l. Hence, type (1) is investigated as an idealistic case. Only two inversions are performed with virtual errors of type (1).

We first describe inversions of artificial data 1. The first result shown in figure 3 was obtained by an inversion with the trade-off parameter $\varepsilon = 3\times10^{-5}$. We assumed virtual uncertainties of type (1): we added uniformly one percent relative errors to the computed artificial data. A typical uncertainty in the rotation rate is about 50 nHz, which is quite large. From this figure, we can see that the solution well recovers the model rate down to a depth of $r/R \simeq 0.3$ or deeper, even though the results are quite sensitive to any virtual data error. The result shown in figure 4 was obtained with the trade-off parameter $\varepsilon = 3\times10^{-5}$, and with virtual uncertainties of type (2) described above. The difference between figures 3 and 4 comes from a difference in the setting of the statistical errors. Since the real observational data of the rotational splittings have large uncertainties at low l, the splitting kernels of the low l modes have smaller weighting factors. It is therefore quite natural that the resolution was low at the deeper region. In figure 4, we can see that the inverted rate deviates significantly from the model rate at radii deeper than $r/R \simeq 0.4$. Since the amplitudes of the splitting kernels are too small to be useful probes in the deep zone, the main factors determining the solution in the deeper zone are the rotation rate at $r/R \simeq 0.4$ and the flatness condition. If the rotation rate at $r/R \simeq 0.4$ shows no significant angular dependence, these factors would cause a flat rotational rate. However, the rotation rate actually found at $r/R \simeq 0.4$ shows a substantial angular dependence. In this case, the flatness condition works to produce a rotation rate that decreases with depth at the equatorial zone and increases with depth at the polar region, as shown in figure 4. It is also evident that the deviation begins at a smaller depth at higher latitude. This is a result of omitting modes with small m from the analysis. Since the eigenmodes providing us with information for the polar region have low m, omitting many of

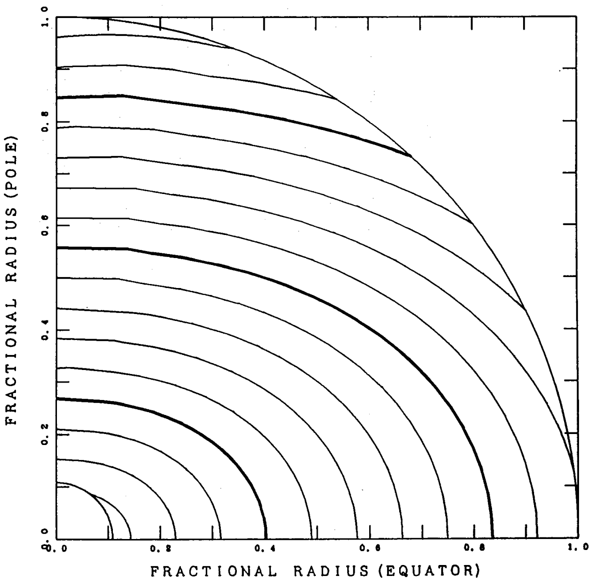

Fig. 1. The contour map of the model rotaiton rate given in equation (5.1). The contour lines are drawn for 16 levels: from 360 nHz to 660 nHz with a step of 20 nHz. Thick curves are the contours for 400 nHz, 500 nHz, and 600 nHz.

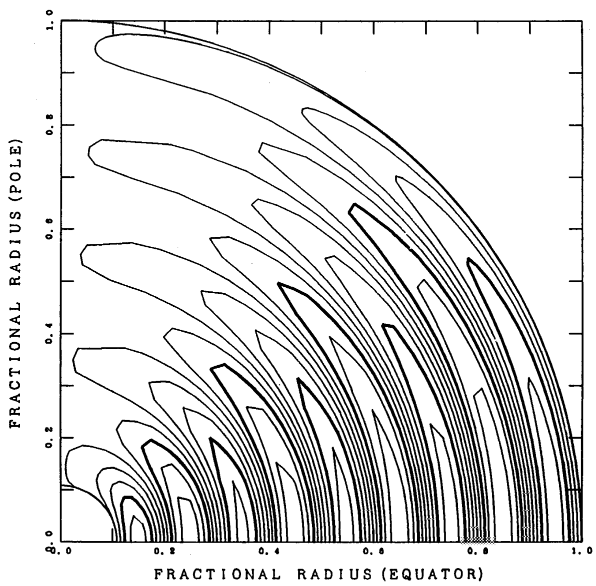

Fig. 2. The contour map of the model rotation rate given in equation (5.2). The contour lines are drawn for 9 levels: from 380 nHz to 540 nHz with a step of 20 nHz. Thick curves are the contours for 400 nHz and 500 nHz.

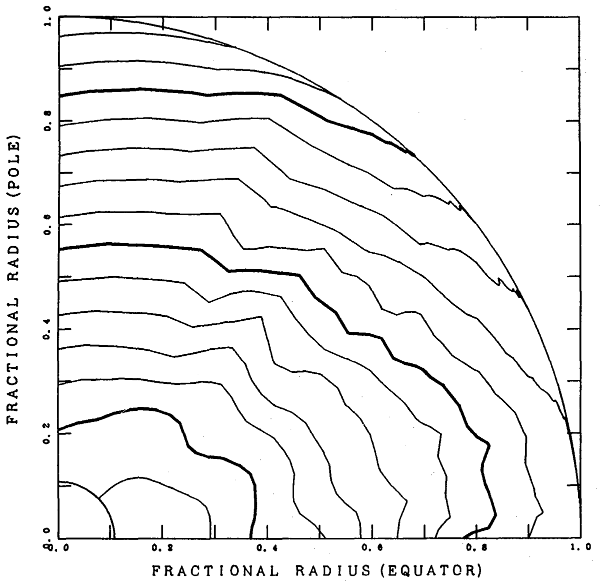

Fig. 3. The contour map of the rotation rate inverted from the artificial data 1 with $\varepsilon = 3 \times 10^{-5}$. Statistical errors are artificially set to be uniformly one per cent. The contour lines are drawn for 14 levels: from 360 nHz to 620 nHz with a step of 20 nHz. Thick curves indicate 400 nHz, 500 nHz, and 600 nHz.

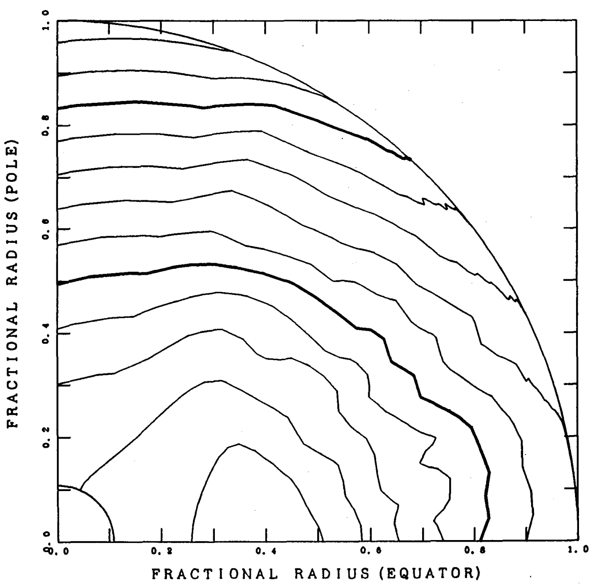

Fig. 4. The contour map of the rotation rate inverted from the artificial data 1 with $\varepsilon = 3 \times 10^{-5}$. The contour lines are drawn for 12 levels: from 360 nHz to 580 nHz with a step of 20 nHz. Thick curves indicate 400 nHz, 500 nHz, and 600 nHz.

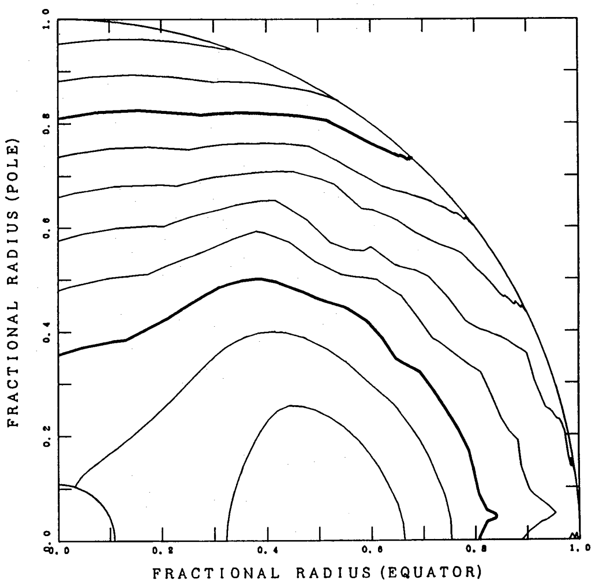

Fig. 5. The contour map of the rotation rate inverted from the artificial data 1 with $\varepsilon = 3 \times 10^{-4}$. The contour lines are drawn for 11 levels: from 360 nHz to 560 nHz with a step of 20 nHz. Thick curves indicate 400 nHz and 500 nHz.

them leads to a low resolution power in the high latitudes. The results obtained by using larger ε are shown in figures 5 ($\varepsilon = 3 \times 10^{-4}$), 6, 7a, 7b ($\varepsilon = 5 \times 10^{-4}$), and 8 ($\varepsilon = 10^{-3}$). We found that $\varepsilon = 3 \times 10^{-3}$ is too large. By inspecting figures 4–8, we confirmed the following tendency: With an increase of the trade-off parameter, ε, the results become less sensitive to the data error, while losing resolution at both the deep interior and high latitude zones.

Since the present inversion technique imposes a smoothness of the rotation rate, inversions of the rotational splittings by using artificial data 2 represent severe tests. The first result shown in figure 9 was obtained by an inversion with the trade-off parameter $\varepsilon = 3 \times 10^{-5}$. The process of the inversion was slightly different from the other inversions: the equation for the boundary constraint was weighted by factor of 10, in order to stabilize the result strongly near the surface. Virtual errors of type (1) were assumed. Comparing figures 2 and 9, we can see that the ridge structure was well detected for $0.3 \lesssim r/R \lesssim 0.9$, though some spurious peaks and dips are also seen here and there. On the other hand, the amplitude of the radial variation is somewhat suppressed. We also performed inversions without such a device, varying the trade-off parameter from 3×10^{-5} to 3×10^{-3}. The result shown in figure 10 is one of them, obtained for $\varepsilon = 5 \times 10^{-4}$. Virtual errors of the type (2) were assumed. For $\varepsilon = 3 \times 10^{-3}$, it was apparent that the trade-off parameter was too large and the result was oversmoothed. By adopting smaller trade-off parameters, we can detect the ridge structures more finely and over wider areas. However, good resolution was not obtained for $r/R \lesssim 0.5$ and $\phi \gtrsim 60°$ for any value of ε. As was the case in the inversions of artificial data 1, the poor resolution at the deepest region is a consequence of a

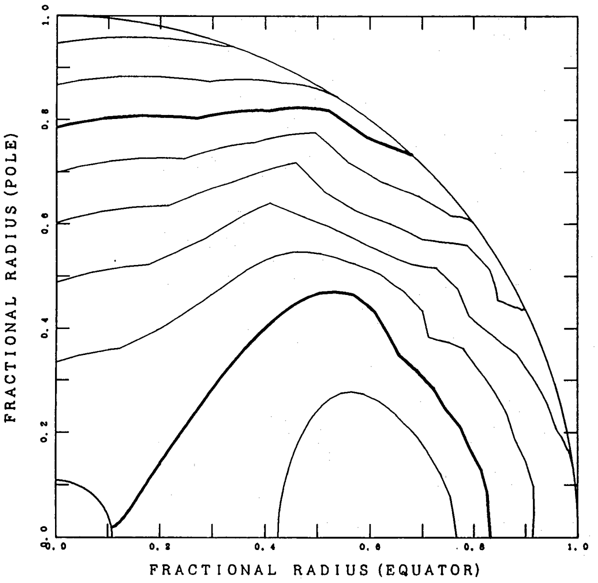

Fig. 6. The contour map of the rotation rate inverted from the artificial data 1 with $\varepsilon = 5 \times 10^{-4}$. The contour lines are drawn for 9 levels: from 360 nHz to 520 nHz with a step of 20 nHz. Thick curves are for 400 nHz and 500 nHz.

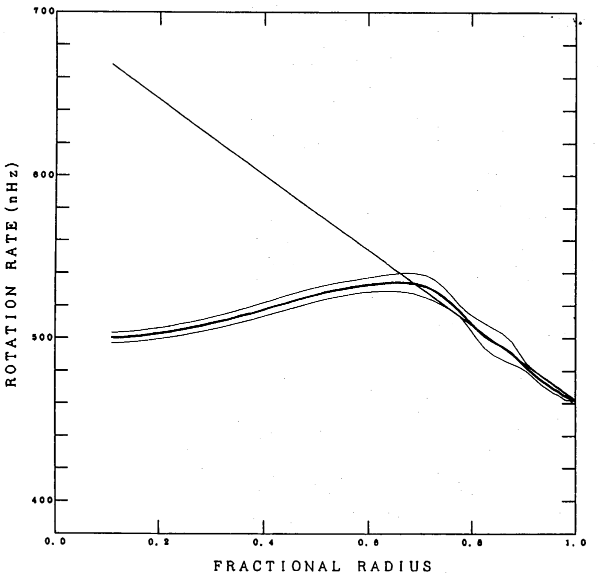

Fig. 7a. The thick curve shows rotation rate shown in figure 6 versus radius at latitude $\theta = 0°$. The straight thin line shows the model rate given in (5.1). Between thin curves lies $\pm 1\sigma$ range.

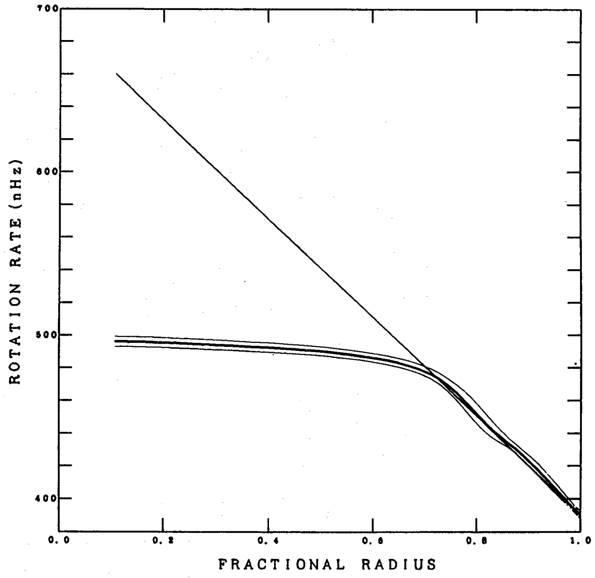

Fig. 7b. The same as figure 7a, but for $\theta = 52°$.

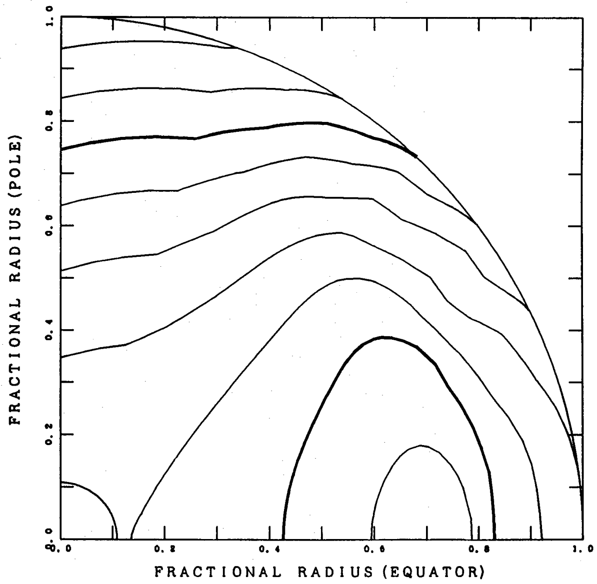

Fig. 8. The contour map of the rotation rate inverted from the artificial data 1 with $\varepsilon = 10^{-3}$. The contour lines are drawn for 9 levels: from 360 nHz to 520 nHz with a step of 20 nHz. Thick curves are for 400 nHz and 500 nHz.

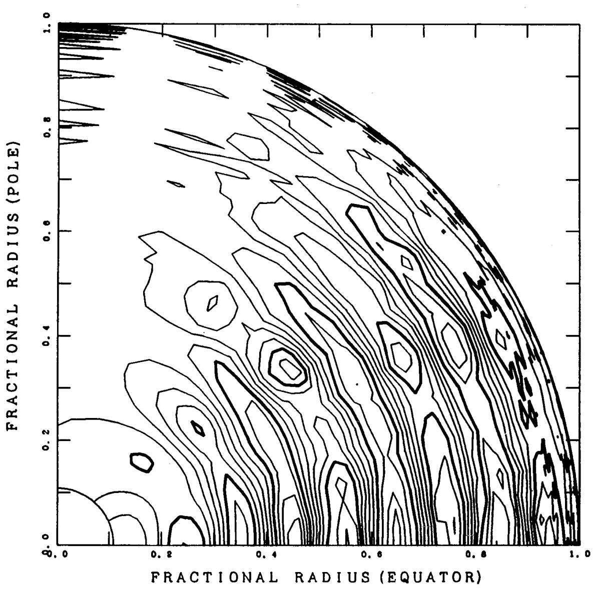

Fig. 9. The contour map of the rotation rate inverted from the artificial data 2 with $\varepsilon = 3 \times 10^{-5}$. Boundary constraints are weighted by a factor 10. The contour lines are drawn for 11 levels: from 360 nHz to 560 nHz with a step of 20 nHz. Thick curves are for 400 nHz and 500 nHz.

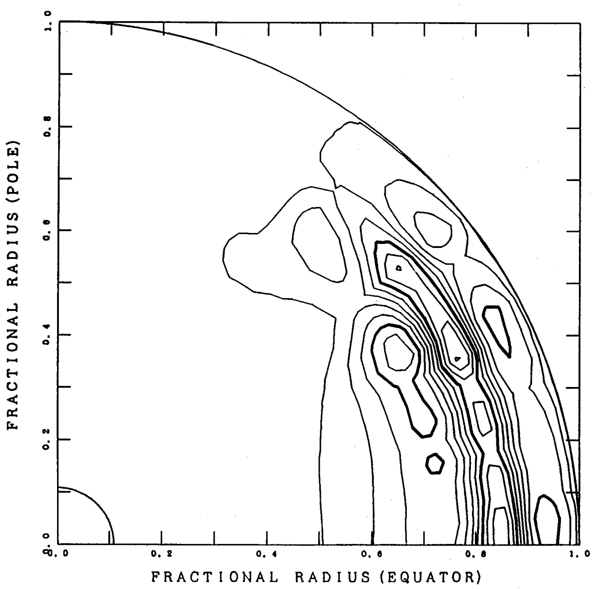

Fig. 10. The contour map of the rotation rate inverted from the artificial data 2 with $\varepsilon = 5 \times 10^{-4}$. The contour lines are drawn for 10 levels: from 380 nHz to 560 nHz with a step of 20 nHz. Thick curves are for 400 nHz and 500 nHz.

deficiency in accurate splitting data for low-degree modes which penetrate to that depth, while omitting modes with low m results in poor resolution at high latitudes.

It is reasonable that in the numerical experiments mentioned above the best resolution was obtained in the range $0.6 \lesssim r/R \lesssim 0.9$ and $0° \lesssim \phi \lesssim 45°$. The resolution of our mesh is insufficient to reveal any independence of the modes near the surface. Hence, the resolution near the surface is poor in our case.

In those figures we find that the contour lines are almost perpendicular to the equatorial plane, although we solved the problem only in a hemisphere, and did not impose such a smooth connection through the equatorial plane. This feature is consistent with our prejudice and provides another support to the validity of the present inversion method near the equator.

5.2. Inversions of the Observed Data

Inversions of the observed splitting data were carried out with five different values of the trade-off parameter, ranging from 3×10^{-3} to 10^{-4}, though we present only three of them below.

From the numerical simulation with the same range of ε, we have learned that reliable solutions are obtained for $r/R \gtrsim 0.7$ for $\varepsilon = 5 \times 10^{-4}$ and for $r/R \gtrsim 0.6$ for $\varepsilon = 10^{-4}$, both at low latitudes. For $\varepsilon = 10^{-3}$, the results are only qualitatively reliable for $r/R \gtrsim 0.75$. That is, even though the broad features were well recovered in the region, since the systematic error exceeds the statistical error, error estimation taking acount only of statistical uncertainty is almost useless. Figure 11 shows the result in the case of $\varepsilon = 10^{-3}$. The global structure is such that with increasing depth the rotation becomes slower at low latitudes and faster at high latitudes, as can be seen in figure 12 in which the rotation rates at $\theta = 0°, 15°, 32°$, and $52°$ are shown as functions of r. The thin curves in figure 12 show the $\pm 1\sigma$ confidence level. The response to statistical errors is weak because of the large value of ε. Some additional features can also be seen. The contour lines in figure 11 are distorted in the vicinity of the depth $r/R \simeq 0.85$. These correspond to a dip in the rotation rate shown in figure 12. We also find that in the low-latitude region the rotation rate reaches its maximum at $r/R \simeq 0.95$. This feature was seen even in the result for $\varepsilon = 3 \times 10^{-3}$, which is not shown. Inversions with smaller values of ε result in similar features, though spurious oscillatory variation appears and the results responded more wildly to data errors. Figures 13 and 14 show the results in the case of $\varepsilon = 5 \times 10^{-4}$. The general trend is the same as that shown in figure 12, except for in the mid-latitude zone. Finer structures are seen when $\varepsilon = 3 \times 10^{-4}$, as can be seen in figure 15, though statistical significances are not high, as in figure 16.

Let us define the residual E^2 as

$$E^2 \equiv \sum_{i=1}^{M} \left(\frac{\delta\omega_i - \sum_{j=1}^{N} K_{ij} \Omega_j}{\Delta\delta\omega_i} \right)^2 . \tag{5.3}$$

We computed E^2 for the inverted rotation rates and obtained $E^2 = 1.31$ for $\varepsilon = 10^{-3}$, $E^2 = 1.16$ for $\varepsilon = 5 \times 10^{-4}$ and $E^2 = 1.14$ for $\varepsilon = 3 \times 10^{-4}$.

Considering the resolving power estimated from numerical simulations, we con-

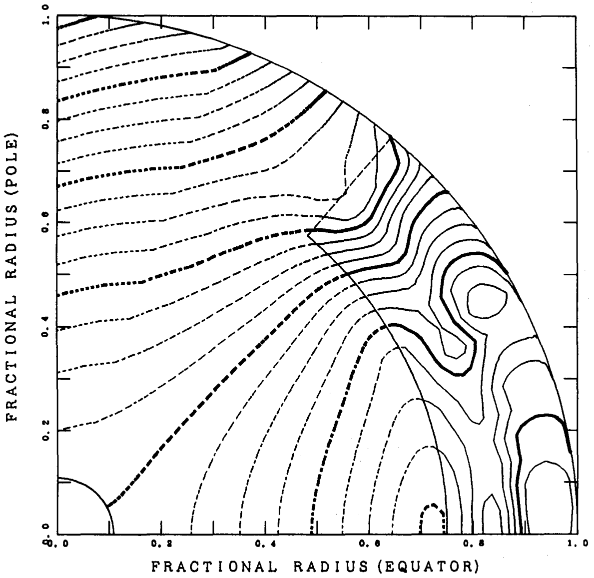

Fig. 11. The contour map of the rotation rate inverted from the observed frequency splittings (Libbrecht 1989) with $\varepsilon = 10^{-3}$. The contour lines are drawn for 27 levels: from 340 nHz to 470 nHz, with a step of 5 nHz. Thick curves are for from 340 nHz to 460 nHz with a step of 20 nHz. Outside the region enclosed by dashed curve, the solution is mainly determined by flatness condition, where the contour lines are drawn as dotted lines.

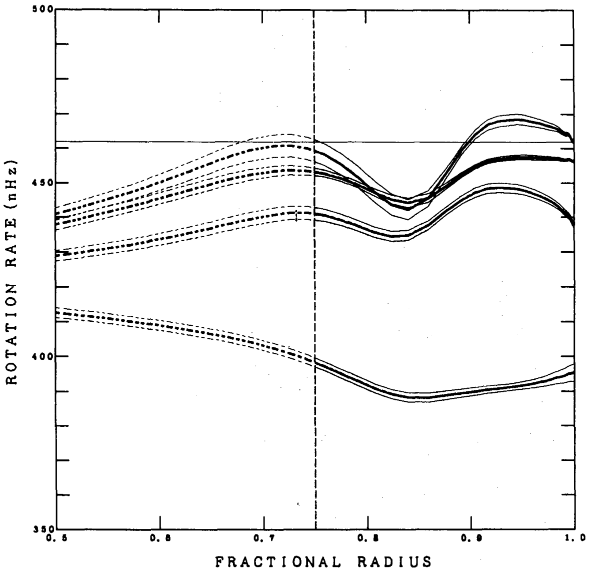

Fig. 12. The thick curves show rotation rate in figure 11 versus radius at latitudes $\theta = 0°$ (uppermost), 15°, 32°, and 52° (lowermost). The thin curves indicate $\pm 1\sigma$ confidence levels. In the region $r/R \lesssim 0.65$, the solution is mainly determined by flatness condition, where the rotation curves are plotted as dotted lines. The thin horizontal line shows the surface rate.

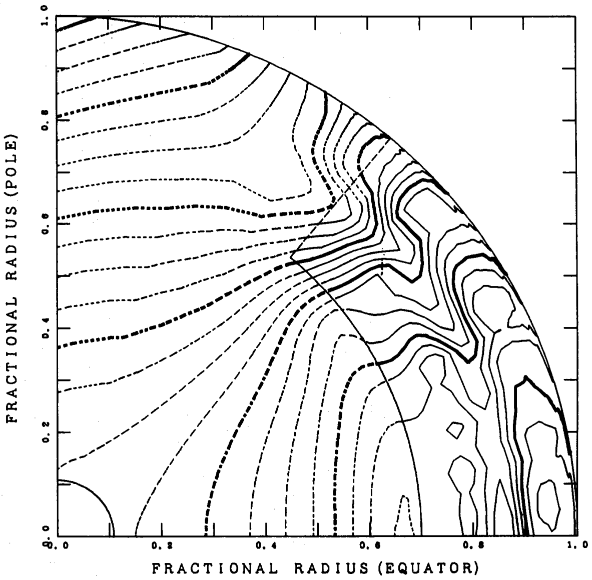

Fig. 13. The contour map of the rotation rate inverted from the observed frequency splittings (Libbrecht 1989) with $\varepsilon = 5 \times 10^{-4}$. The contour lines are drawn for 27 levels: from 340 nHz to 470 nHz, with a step of 5 nHz. Thick curves are for from 340 nHz to 460 nHz with a step of 20 nHz. Outside the region enclosed by dashed curve, the solution is mainly determined by flatness condition, where the contour lines are drawn as dotted lines.

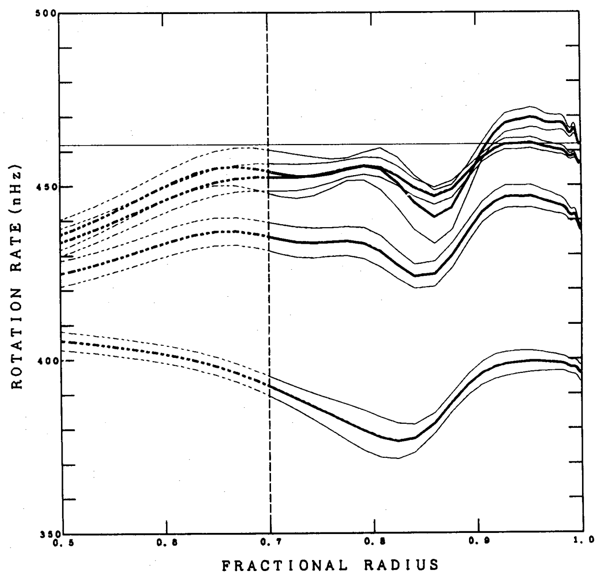

Fig. 14. The thick curves show rotation rate in figure 13 versus radius at latitudes $\theta = 0°$ (uppermost), 15°, 32°, and 52° (lowermost). The thin curves indicate $\pm 1\sigma$ confidence levels. In the region $r/R \lesssim 0.65$, the solution is mainly determined by flatness condition, where the rotation curves are plotted as dotted lines. The thin horizontal line shows the surface rate.

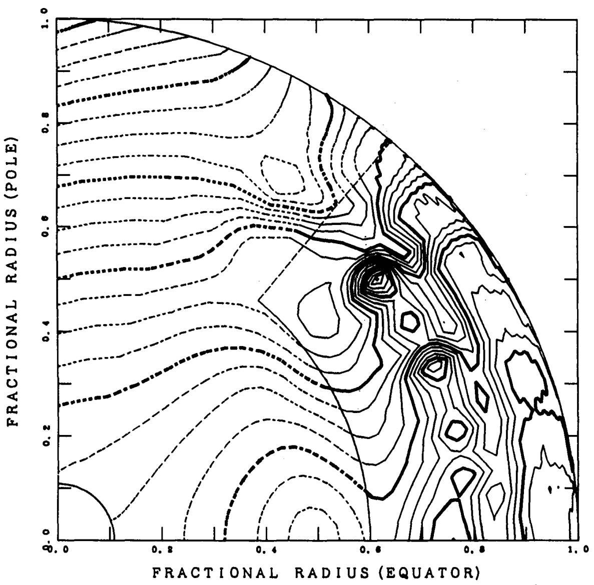

Fig. 15. The contour map of the rotation rate inverted from the observed frequency splittings (Libbrecht 1989) with $\varepsilon = 3 \times 10^{-4}$. The contour lines are drawn for 26 levels: from 340 nHz to 465 nHz, with a step of 5 nHz. Thick curves are for 340 nHz to 460 nHz with a step of 20 nHz. Outside the region enclosed by dashed curve, the solution is mainly determined by flatness condition, where the contour lines are drawn as dotted lines.

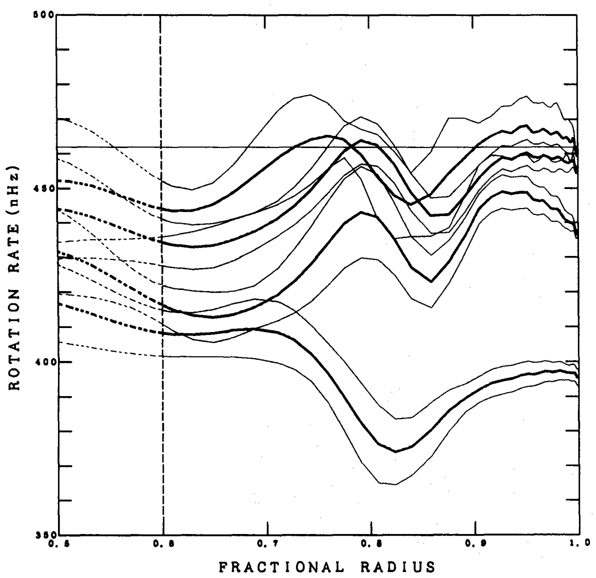

Fig. 16. The thick curves shows rotation rate in figure 15 versus radius at latitudes $\theta = 0°$ (uppermost), 15°, 32°, and 52° (lowermost). The thin curves indicate $\pm 1\sigma$ confidence levels. In the region $r/R \lesssim 0.65$, the solution is mainly determined by flatness condition, where the rotation curves are plotted as dotted lines. The thin horizontal line shows the surface rate.

clude that the rotation rate in the low-latitude region is slightly faster than the surface rotation rate in the outer ten percent in radius and decreases to the level about five percent lower than the surface in the lower half of the convection zone. All of the inversion results with various values of ε indicated a dip around a depth of $r/R \simeq 0.85$ and a slight increment in the rotation rate at a depth of $r/R \simeq 0.95$ in the low-latitude region. The latter feature may be lost if we adopt the higher rotation rate at the surface as the boundary constraint. However, since Snodgrass' (1983) value is among the highest at the low-latitude zone, the latter feature will survive for any realistic boundary condition. In the deeper region, the rotation rate in the low-latitude zone is as fast as the surface rate in the region $0.70 < r/R < 0.80$, but seems to become slower than the surface rate in $r/R < 0.70$. The rotation rate at high latitude decreases with depth in the outer twenty percent in radius, and then gradually increases. This implies a rotation rate faster than the surface rate at $r/R \lesssim 0.70$. Besides these features, roughly speaking, the rotation rate seems to hold differential rotation at the surface in the upper half of the convection zone and to show only a small deviation from rigid rotation in the deep interior.

Even though a really quantitative estimate of the rotation rate at $r/R \lesssim 0.7$ is impossible, the present results show that a latitudinal variation of the rotation rate tends to decrease at $r/R \sim 0.7$. Besides, we know that the latitudinal variation must vanish at the center. These two facts imply that the latitudinal variation tends to decrease for $r/R \lesssim 0.7$.

6. Discussion

Christensen-Dalsgaard and Schou (1988) as well as Dziembowski et al. (1989) also inverted the same data set (see also Libbrecht 1988). Both of them expanded the rotational rate, $\Omega(r, \theta)$, in terms of $\cos^2 \theta$ in the form of equation (2.21), and searched for $\Omega_0(r)$, $\Omega_2(r)$, and $\Omega_4(r)$. To obtain these, the former group performed inversion by an optimal averaging method, while the latter group adopted a least-squares technique with regularization.

The present inversion results are consistent with theirs regarding the point that the rotation rate at a low-latitude zone has a dip near $r/R \simeq 0.85$. However, there is also an inconsistency. Christensen-Dalsgaard and Schou (1988) as well as Dziembowski et al. (1989) claimed that they found a steep gradient of the rotation rate on the equatorial plane at the bottom of the convection zone. In the present results, such a feature is seen only in the case where $\varepsilon = 10^{-4}$, and is never seen in cases of a larger value of ε.

In general, the present inversion results look like a combination of the results of Dziembowski et al. (1989) with two different values of their trade-off parameter, which controls smoothness of their solutions, as does λ in equation (2.7). The outer part ($r/R \gtrsim 0.8$) looks like their less-smoothed result, while the inner part ($r/R \lesssim 0.8$) looks like their more-smoothed result. In order to reproduce their less-smoothed result, we must adopt the smallest value of ε among the values that we examined. This simply means that the sensitivity is dependent on the inversion methods. First, the standard regularization method which they adopted suppresses any non-smooth feature, while the present method allows such a feature if that feature is buried in data associated with large singular values. Of course, this means that their results reflect the data that are associated with small singular values, while we neglect them completely and, as a result, use only a part of the data. Second, they adopted expansion (2.8) and suppressed derivatives of $\Omega_0(r), \Omega_1(r)$, and $\Omega_2(r)$, while we suppressed $|\nabla\Omega(r,\theta)|$. Suppressing derivatives of $\Omega_1(r)$ or $\Omega_2(r)$, instead of their amplitudes, can result in a larger angular gradient than that obtained by suppressing $|\nabla\Omega(r,\theta)|$. On the other hand, expansion (2.8) guarantees a smooth angular gradient which our method does not necessarily provide.

The currently available observational data provide us information only up to a_5 of the expansion coefficients in equation (4.1). This means that the current data are not sufficiently accurate for a fully two-dimensional inversion, like that in the present work. However, many future observational plans have been proposed, some of which are very appropriate for very accurate measurements of rotational splittings. The fully two-dimensional approach adopted in the present work is more appropriate for the inversion of such a highly accurate measurement of rotational splittings. In fact, it is simpler than the parametrization methods if we can afford to include so many parametrized terms or mesh points. Since Libbrecht's (1989) data are more accurate for higher degree modes than for lower degree modes, error-weighted splitting kernels have quite small amplitudes in the inner part.

In the present work small singular values are discarded. This means that rotation data in the inner part is disregarded and replaced by the flatness condition. On the other hand, large singular values are retained so that the rotation data in the outer part are not discarded. The low resolution at high latitudes is mainly caused by the fact that we had to omit many of the low-m modes with high degree l because the mesh size is limited to 100×20. In order to improve resolution, we must set finer meshes, which require correspondingly more computer memory, or finer numerical techniques.

Korzennik et al. (1990) performed an inversion of their own data obtained at Mt. Wilson. Their perliminary result in the equatorial plane is roughly consistent with the persent work. It is interesting that they detected a small increment of the rotation rate below the photosphere, which was not found by others who analyzed the same data set as we used.

Brown et al. (1989) presented their inference concerning the rotation rate in the sun, using the data of Brown and Morrow (1987). They reported that in the convection zone the radial gradient of the rotation rate is fairly small, which seems to conflict with the standard $\alpha - \omega$ dynamo theory. The present results are generally in agreement with theirs, but do not exclude the possibility of a large radial gradient of rotation rate in the convection zone. In figures 11–16 we find that the radial gradient can even be negative, which is required by the standard $\alpha - \omega$ dynamo, but only in the middle of the convection zone at low- to mid-latitudes.In fact, in our results the rotation rate at the bottom of convection zone does not exceed the surface rate by as much as theirs.

The solar internal rotation is considered to be an important factor for determining solar activity and, hence, it is expected to vary during the solar cycle. To see such a time variation, we plan to apply the present method with the same parameters to Libbrecht and Woodard's (1990) new data set obtained in 1988 using the same instruments and techniques as for Libbrecht's (1989) 1986 data.

The numerical computations were performed partly by FACOM VP200 at the Institute of Space and Astronautical Science, and by FACOM M780 at the National Astronomical Observatory.

References

Brown, T. M., Christensen-Dalsgaard, J., Dziembowski, W. A., Goode, P., Gough, D. O., and Morrow, C. A. 1989, *Astrophys. J.*, **343**, 526.

Brown, T. M., and Morrow, C. A. 1987, *Astrophys. J. Letters*, **314**, L21.

Christensen-Dalsgaard, J., Duvall, T. L., Jr., Gough, D. O., Harvey, J. W., and Rhodes, E. J., Jr. 1985, *Nature*, **315**, 378.

Christensen-Dalsgaard, J., Gough, D. O., and Thompson, M. 1988, in *Seismology of the Sun and Sun-like Stars*, ed. E. Rolfe, ESA SP-286 (ESA Publication Division, Noordwijk), p. 493.

Christensen-Dalsgaard, J., and Schou, J. 1988, in *Seismology of the Sun and Sun-like Stars*, ed. E. Rolfe, ESA SP-286 (ESA Publication Division, Noordwijk), p. 149.

Craig, I. J. D., and Brown, J. C. 1986, *Inverse Problems in Astronomy* (Adam Hilger Ltd., Bristol).

Duvall, T. L., Jr., Dziembowski, W. A., Goode, P. R., Gough, D. O., Harvey, J. W., and Leibacher, J. W. 1984, *Nature*, **310**, 22.

Duvall, T. L., Jr., and Harvey, J. W. 1984, *Nature*, **310**, 19.

Dziembowski, W. A., Goode, P. R., and Libbrecht, K. G. 1989, *Astrophys. J. Letters*, **337**, L53.

Dziembowski, W. A., Pamjatnykh, A. A., and Sienkiewicz, R., 1990, *Monthly Notices Roy. Astron. Soc.*, **244**, 542.

Forsythe, G. E., Malcolm, M. A., and Moler, C. B. 1977, *Computer Methods for Mathematical Computations* (Prentice-Hall, Englewood Cliffs, New Jersey).

Gabriel, M., and Namry, F. 1986, in *Seismology of the Sun and Distant Stars*, ed. D. O. Gough (D. Reidel Publishing Company, Dordrecht), p. 243.

Goode, P. R., Dziembowski, W. A., Rhodes, E. J., Jr., and Korzennik, S. 1990, in *Progress of Seismology of the Sun and Stars*, ed. Y. Osaki and H. Shibahashi (Springer-Verlag, Berlin), p. 349.

Gough, D. 1985, *Solar Physics*, **100**, 65.

Gough, D. O. 1984, *Phil. Trans. Roy. Soc. Lond.*, **A313**, 27.

Gough, D. O., and Kosovichev, A. G. 1988, in *Seismology of the Sun and Sun-like Stars*, ed. E. Rolfe, ESA SP-286 (ESA Publication Division, Noordwijk), p. 195.

Hansen, C. J., Cox, J. P., and van Horn, H. M. 1977, *Astrophys J.*, **217**, 151.

Howard, R., Adkins, J. M., Boyden, J. E., Cragg, T. A., Gregory, T. S., Labonte, B. J., Padilla, S. P., and Webster, L. 1983, *Solar Physics*, **83**, 321.

Jeffrey, W. 1988, *Astrophys. J.*, **327**, 987.

Korzennik, S. G., Cacciani, A., Rhodes, E. J., Jr., Tomczyk, S., and Ulrich, R. K. 1988, in *Seismology of the Sun and Sun-like Stars*, ed. E. Rolfe, ESA SP-286 (ESA Publication Division, Noordwijk), p. 117.

Korzennik, S. G., Cacciani, A., Rhodes, E. J., Jr., and Ulrich, R. K. 1990, in *Progress of Seismology of the Sun and Stars*, ed. Y. Osaki and H. Shibahashi (Springer-Verlag, Berlin), p. 341.

Libbrecht, K. G. 1985, *Solar Physics*, **99**, 371.

Libbrecht, K. G. 1988, in *Seismology of the Sun and Sun-like Stars*, ed. E. Rolfe, ESA SP-286 (ESA Publication Division, Noordwijk), p. 131.

Libbrecht, K. G. 1989, *Astrophys. J.*, **336**, 1092.
Libbrecht, K. G., and Woodard, M. F. 1990, in *Progress of Seismology of the Sun and Stars*, ed. Y. Osaki and H. Shibahashi (Springer-Verlag, Berlin), p. 145.
Parker, R. L. 1977, *Ann. Rev. Earth Planet. Sci.*, **5**, 35.
Phillips, D. L. 1962, *J. Ass. Comput. Mach.*, **9**, 84.
Rao, C. R., and Mitra, S. K. 1971, *Generalized Inverse Matrices and Its Applicctions* (Wiley and Sons, New York).
Rhodes, E. J., Jr., Cacciani, A., and Korzennik, S. G. 1990, in *Progress of Seismology of the Sun and Stars*, ed. Y. Osaki and H. Shibahashi (Springer-Verlag, Berlin), p. 163.
Rhodes, E. J., Jr., Cacciani, A., Korzennik, S. G., Tomczyk, S., Ulrich, R. K., and Woodard, M. F. 1988, in *Seismology of the Sun and Sun-like Stars*, ed. E. Rolfe, ESA SP-286 (ESA Publication Division, Noordwijk), p. 73.
Sekii, T. 1990, in *Progress of Seismology of the Sun and Stars*, ed. Y. Osaki and H. Shibahashi (Springer-Verlag, Berlin), p. 337.
Sekii, T., and Shibahashi, H. 1988, in *Seismology of the Sun and Sun-like Stars*, ed. E. Rolfe, ESA SP-286, (ESA Publication Division, Noordwijk), p. 521.
Shibahashi, H., Noels, A., and Gabriel, M. 1983, *Astron. Astrophys.*, **123**, 283.
Shibahashi, H., and Sekii, T. 1988, in *Seismology of the Sun and Sun-like Stars*, ed. E. Rolfe, ESA SP-286 (ESA Publication Division, Noordwijk), p. 471.
Snodgrass, H. B. 1983, *Astrophys. J.*, **270**, 288.
Stenflo, J. O. 1989, *Astron. Astrophys.*, **210**, 403.
Tikhonov, A. N. 1963, *Sov. Maths-Dokl.*, **4**, 1035.
Twomey, S. 1963, *J. Ass. Comput. Mach.*, **10**, 97.
Unno, W., Osaki, Y., Ando, H., Saio, H., and Shibahashi, H. 1989, *Nonradial Oscillations of Stars* (University of Tokyo Press, Tokyo).
Vorontsov, S. V. 1988, in *Seismology of the Sun and Sun-like Stars*, ed E. Rolfe, ESA SP-286 (ESA Publication Division, Noordwijk), p. 475.
Vorontsov, S. V., and Shibahashi, H. 1990, in *Progress of Seismology of the Sun and Stars*, ed. Y. Osaki and H. Shibahashi (Springer-Verlag, Berlin), p. 325.